

**Nonlinear elastic behavior of two-dimensional molybdenum disulfide**Ryan C. Cooper,<sup>1</sup> Changgu Lee,<sup>2</sup> Chris A. Marianetti,<sup>3</sup> Xiaoding Wei,<sup>4</sup> James Hone,<sup>1</sup> and Jeffrey W. Kysar<sup>1</sup><sup>1</sup>*Department of Mechanical Engineering, Columbia University, New York, NY 10027, USA*<sup>2</sup>*Department of Mechanical Engineering, Sungkyunkwan University, Seoul, Korea*<sup>3</sup>*Department of Applied Physics and Applied Mathematics, Columbia University, New York, NY 10027, USA*<sup>4</sup>*Department of Mechanical Engineering, Northwestern University, Evanston, IL 60201*

(Received 16 May 2012; published 22 January 2013; corrected 31 January 2013)

This research explores the nonlinear elastic properties of two-dimensional molybdenum disulfide. We derive a thermodynamically rigorous nonlinear elastic constitutive equation and then calculate the nonlinear elastic response of two-dimensional MoS<sub>2</sub> with first-principles density functional theory (DFT) calculations. The nonlinear elastic properties are used to predict the behavior of suspended monolayer MoS<sub>2</sub> subjected to a spherical indenter load at finite strains in a multiple-length-scale finite element analysis model. The model is validated experimentally by indenting suspended circular MoS<sub>2</sub> membranes with an atomic force microscope. We find that the two-dimensional Young's modulus and intrinsic strength of monolayer MoS<sub>2</sub> are 130 and 16.5 N/m, respectively. The results approach Griffith's predicted intrinsic strength limit of  $\sigma_{\text{int}} \sim \frac{E}{9}$ , where  $E$  is the Young's modulus. This study reveals the predictive power of first-principles density functional theory in the derivation of nonlinear elastic properties of two-dimensional MoS<sub>2</sub>. Furthermore, the study bridges three main gaps that hinder understanding of material properties: DFT to finite element analysis, experimental results to DFT, and the nanoscale to the microscale. In bridging these three gaps, the experimental results validate the DFT calculations and the multiscale constitutive model.

DOI: [10.1103/PhysRevB.87.035423](https://doi.org/10.1103/PhysRevB.87.035423)

PACS number(s): 68.60.Bs, 31.15.E-, 62.20.D-, 81.40.Jj

**I. INTRODUCTION**

Two-dimensional (2D) materials have recently become an area of increased research focus despite their long being considered thermodynamically unstable.<sup>1</sup> The experimental significance of 2D materials was first revealed in 2004 when the electrical properties of graphite crystals limited to only a few atoms thick were probed.<sup>2</sup> These 2D crystals were obtained via the clever and simple mechanical exfoliation method. Since this groundbreaking study, graphene and other 2D materials have been studied in areas of basic research such as electronics, optics, and mechanics.<sup>3-8</sup>

Two-dimensional materials serve as outstanding testbeds for fundamental studies of mechanical properties under extreme strains.<sup>4</sup> They can be fabricated in a pristine condition essentially free of defects, which enables them to achieve extreme tensile strain states prior to fracture or void nucleation. The mechanical flexibility of 2D materials allows them to conform to a surface and adhere to it via van der Waals interactions, thus simplifying the boundary conditions on a 2D material during mechanical characterization.<sup>4</sup> In addition, the relatively small number of atoms per unit cell in known 2D materials offer the opportunity to use first-principles and molecular dynamics computational methods.<sup>9</sup> Finally, the 2D geometry restricts the possible deformation states which render higher-order nonlinear continuum elasticity formulations sufficiently tractable to combine with the atomistic methods to formulate multi-length-scale models that can be readily incorporated into standard finite element analysis (FEA) formulations.<sup>9,10</sup> Most of these previous studies concentrated on monatomically thin graphene, which is a single close-packed atomic plane of a single component (i.e., carbon), but other more general 2D materials can be produced by mechanical exfoliation.<sup>7,11-15</sup>

In this study, we extend these methods to study 2D molybdenum disulfide, which is a multicomponent and multiatomic layer system. Molybdenum disulfide is a layered transition metal dichalcogenide (LTMD) composed of layers of molybdenum atoms sandwiched between sulfur atoms, with each molybdenum atom ionically bonded to six sulfur atoms as seen in Fig. 1. Multiple MoS<sub>2</sub> layers are held together in the bulk material through van der Waals interactions, so the MoS<sub>2</sub> monolayers are easily cleaved.

Molybdenum disulfide has been used as a solid lubricant for centuries and was studied as a material for detecting and rectifying radio signals in the 1950s.<sup>16</sup> Bulk MoS<sub>2</sub> has a hardness of 1–1.5 on the Mohs scale and exhibits excellent lubrication in high vacuum or under atmospheric conditions.<sup>16</sup> A study on bundles of MoS<sub>2</sub> nanotubes reveals a Young's modulus of 120 GPa with an intertube shear modulus of  $160 \pm 30$  MPa.<sup>17</sup> Bulk MoS<sub>2</sub> is an indirect gap semiconductor with a band gap of 1.2 eV, but by reducing the number of layers one can modify the band structure and create a direct gap semiconductor.<sup>5,12,18-21</sup> Recently, monolayers of MoS<sub>2</sub> have been investigated as materials for microelectromechanical systems (MEMS) and nanoelectromechanical systems (NEMS) devices.<sup>5,7,12,17</sup> The low power dissipation of MoS<sub>2</sub> direct gap semiconductors and its low cost make it an ideal candidate for flexible electronic applications. Studies have investigated the crystal structure and electrical properties.<sup>5-7,12,14,16,18,20-22</sup> Finally, the elastic properties of 2D MoS<sub>2</sub> have been investigated to characterize the Young's modulus and breaking strength.<sup>11</sup> However a more complete understanding of the mechanical properties of 2D MoS<sub>2</sub> is necessary to be able to predict its response upon incorporation into MEMS and NEMS devices.

The thickness of a 2D material is indeterminate because its out-of-plane electron configuration may change as a function

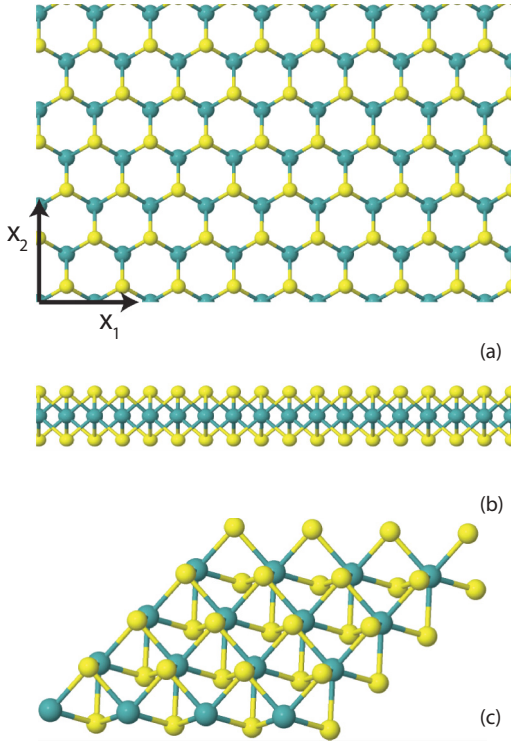


FIG. 1. (Color online) Atomic structure of monolayer MoS<sub>2</sub>. The green and yellow spheres represent Mo and S atoms, respectively: (a) top view of the atomic structure; (b) side view of MoS<sub>2</sub> to highlight the out-of-plane sulfur atoms; and (c) oblique view of 4 × 4 unit cells.

of deformation state. Hence, stress  $\sigma$  and elastic moduli such as Young's modulus  $E$  are defined intrinsically as force per length rather than force per area. For purposes of comparison to three-dimensional (3D) materials, the derived 3D quantities of stress and elastic moduli of a 2D material can be determined as  $\sigma^{3D} = \sigma/t$  and  $E^{3D} = E/t$ , respectively, where  $t$  is an assumed thickness of the 2D materials. Herein, we assume  $t = 0.615$  nm as a representative thickness of 2D MoS<sub>2</sub>, which is the interlayer spacing between layers of MoS<sub>2</sub> in the bulk material.<sup>16</sup> Unless explicitly expressed otherwise with a superscript 3D, we assume all stress and moduli are 2D quantities.

The overall goal of this study is to determine the nonlinear elastic properties of single-layer MoS<sub>2</sub>. First, we derive a thermodynamically rigorous continuum elastic constitutive model of the nonlinear elastic response of MoS<sub>2</sub> via a Taylor series expansion of the elastic strain energy density potential. We then use density functional theory (DFT) to calculate the elastic response of MoS<sub>2</sub> for several in-plane deformation states of uniaxial strain as well as biaxial strain. The magnitude of the applied strains ranges from infinitesimal to finite deformations beyond that corresponding to the intrinsic (i.e., maximum) stress. All components of the stiffness tensors of the higher-order elastic constitutive model are determined by fitting the continuum model to the stress versus strain results of the uniaxial strain deformation states studied by DFT calculations. We use the crystal symmetry of 2D MoS<sub>2</sub> to determine the number of independent elastic constants for the continuum model. To verify the internal consistency of

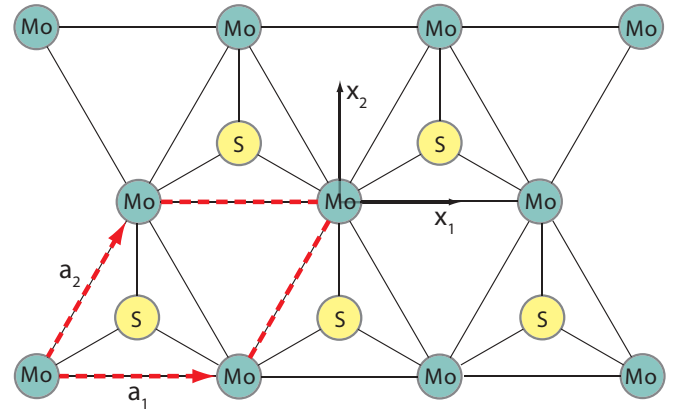


FIG. 2. (Color online) Unit cell of monolayer MoS<sub>2</sub>. The axes are labeled by the black arrows and the unit cell is contained in the dashed red box. Atoms of S lie both above and below the plane of the Mo atoms.

the higher-order continuum theory, we calculate the elastic response with DFT of MoS<sub>2</sub> under a condition of uniaxial stress and demonstrate that the continuum model, fit only to the uniaxial strain DFT results, accurately predicts the DFT results in uniaxial stress. To validate the model, we use atomic force microscopy (AFM) nanoindentation to determine the force-displacement response as well as the force required to rupture a monolayer MoS<sub>2</sub> film suspended over open circular holes. The results of a detailed finite element analysis of the indentation experiments using the nonlinear elastic continuum formulation are consistent with the experimental measurements to within experimental uncertainty, thus validating the model.

## II. NONLINEAR ELASTIC CONSTITUTIVE MODEL

Figure 2 shows the undeformed unit cell of monolayer MoS<sub>2</sub> described by two lattice vectors  $\mathbf{a}_i$  ( $i = 1, 2$ ). Unit vectors in the  $x_1$ - and  $x_2$ -directions relative to Fig. 2 are denoted as  $\hat{\mathbf{e}}_1$  and  $\hat{\mathbf{e}}_2$ , respectively, and  $\mathbf{a}_1 = a_1 \hat{\mathbf{e}}_1$  and  $\mathbf{a}_2 = a_2(\frac{1}{2}\hat{\mathbf{e}}_1 + \frac{\sqrt{3}}{2}\hat{\mathbf{e}}_2)$ . As will be discussed in the following, the magnitudes of the lattice vectors are  $a_1 = a_2 = 3.16$  Å in the undeformed reference configuration.

A macroscopic homogeneous in-plane deformation of the 2D crystal results in deformation of the lattice vectors  $\mathbf{a}'_i = \mathbf{F}\mathbf{a}_i$  where  $\mathbf{F}$  is the deformation gradient tensor and  $\mathbf{a}'_i$  are the deformed lattice vectors. Writing the Lagrangian strain tensor as  $\boldsymbol{\eta} = \frac{1}{2}(\mathbf{F}^T\mathbf{F} - \mathbf{I})$  where  $\mathbf{I}$  is the identity tensor, the strain energy density potential has the functional form  $\Phi = \Phi(\boldsymbol{\eta})$ , which quantifies the elastic strain energy per unit reference area of the undeformed MoS<sub>2</sub>.<sup>9</sup>

The elastic strain energy density potential can be expressed as a Taylor series expansion in powers of strain as

$$\begin{aligned} \Phi = & \frac{1}{2!} C_{ijkl} \eta_{ij} \eta_{kl} + \frac{1}{3!} C_{ijklmn} \eta_{ij} \eta_{kl} \eta_{mn} \\ & + \frac{1}{4!} C_{ijklmnop} \eta_{ij} \eta_{kl} \eta_{mn} \eta_{op} \\ & + \frac{1}{5!} C_{ijklmnopqr} \eta_{ij} \eta_{kl} \eta_{mn} \eta_{op} \eta_{qr} + \dots, \quad (1) \end{aligned}$$

where  $C_{ijkl}$ ,  $C_{ijklmn}$ ,  $C_{ijklmnop}$ , and  $C_{ijklmnopqr}$  are the second-, third-, fourth-, and fifth-order stiffness tensors, respectively;<sup>9</sup> the summation convention is adopted for repeating indices and summation for lower case indices runs from 1 to 3. The quadratic term in strain suffices to describe a linear elastic material, so the higher-order terms are necessary to describe the nonlinear response. The second Piola-Kirchhoff stress tensor  $\Sigma_{ij}$ , defined in terms of its work conjugate Lagrangian strain, is calculated by taking  $\partial\Phi/\partial\eta_{ij}$  to obtain

$$\begin{aligned} \Sigma_{ij} = & C_{ijkl}\eta_{kl} + \frac{1}{2!}C_{ijklmn}\eta_{kl}\eta_{mn} + \frac{1}{3!}C_{ijklmnop}\eta_{kl}\eta_{mn}\eta_{op} \\ & + \frac{1}{4!}C_{ijklmnopqr}\eta_{kl}\eta_{mn}\eta_{op}\eta_{qr} + \dots \end{aligned} \quad (2)$$

Upon adopting the Voigt notation,<sup>23</sup> the stress tensor can be expressed as

$$\begin{aligned} \Sigma_I = & C_{IJ}\eta_J + \frac{1}{2!}C_{IJK}\eta_J\eta_K + \frac{1}{3!}C_{IJKL}\eta_J\eta_K\eta_L \\ & + \frac{1}{4!}C_{IJKLM}\eta_J\eta_K\eta_L\eta_M + \dots, \end{aligned} \quad (3)$$

where the lower case indices transform to Voigt indices in upper case letters as  $11 \rightarrow 1$ ,  $22 \rightarrow 2$ ,  $33 \rightarrow 3$ ,  $23 \rightarrow 4$ ,  $13 \rightarrow 5$ , and  $12 \rightarrow 6$ ; the summation convention still holds and summation of upper case indices ranges from 1 to 6. The components of  $C_{IJ}$  are the second-order elastic constants (SOEC), those of  $C_{IJK}$  are the third-order elastic constants (TOEC), those of  $C_{IJKL}$  are the fourth-order elastic constants (FOEC), and those of  $C_{IJKLM}$  are the fifth-order elastic constants (FFOEC).

A general anisotropic elastic solid has 21 independent components in the SOEC, 56 in the TOEC, 126 in the FOEC, and 252 in the FFOEC. The deformation state of a 2D material can be approximated as being solely an in-plane deformation state when the contribution of bending deformation to the

strain energy density is negligible compared to that of in-plane deformation. This implies that only in-plane components (i.e., those with indices that include only  $I, J = 1, 2$  and 6 or  $i, j = 1$  and 2) of the stiffness tensors may be nonzero, and all out-of-plane components of the stiffness tensors are identically zero. An undeformed 2D MoS<sub>2</sub> monolayer has point group  $D_{3h}$ , which has a hexagonal crystal structure.<sup>13,24</sup> Previous studies have shown that in-plane deformation states for this point group have two independent components of the SOEC, three independent components of the TOEC tensor, and four independent components of the FOEC tensor.<sup>25,26</sup> We calculate that the FFOEC tensor has five independent nonzero components by imposing the symmetry elements of monolayer MoS<sub>2</sub> symmetry on the tensor based upon

$$\begin{aligned} C_{abcdefghij} \\ = & Q_{ka} Q_{lb} Q_{mc} Q_{nd} Q_{oe} C_{klmnopqrst} Q_{pf} Q_{qg} Q_{rh} Q_{si} Q_{tj}, \end{aligned} \quad (4)$$

where  $\mathbf{Q}$  refers to the transformation matrix associated with a symmetry element. Thus, monolayer MoS<sub>2</sub> requires a total of only 14 independent components of the stiffness tensors to describe finite in-plane deformations. The list of elastic constants is given in Table I.

For general infinitesimal in-plane deformations, the elastic response is isotropic and linear with Young's modulus  $E = (C_{11}^2 - C_{12}^2)/C_{11}$  and Poisson's ratio  $\nu = C_{12}/C_{11}$  and the full linear-elastic response is

$$\begin{bmatrix} \Sigma_1 \\ \Sigma_2 \\ \Sigma_6 \end{bmatrix} = \begin{bmatrix} C_{11} & C_{12} & 0 \\ C_{12} & C_{11} & 0 \\ 0 & 0 & \frac{C_{11}-C_{12}}{2} \end{bmatrix} \begin{bmatrix} \eta_1 \\ \eta_2 \\ \eta_6 \end{bmatrix}. \quad (5)$$

For general finite in-plane deformations, the elastic response is anisotropic and nonlinear and the in-plane components of the second Piola-Kirchhoff tensor  $\Sigma_1$ ,  $\Sigma_2$ , and  $\Sigma_6$  are given by

$$\begin{aligned} \Sigma_1 = & C_{11}\eta_1 + C_{12}\eta_2 + \frac{1}{2}C_{111}\eta_1^2 + C_{112}\eta_1\eta_2 - \frac{1}{2}(\frac{1}{2}C_{111} + \frac{1}{4}C_{112} - \frac{3}{4}C_{222})\eta_6^2 + \frac{1}{2}(C_{111} + C_{112} - C_{222})\eta_2^2 \\ & + \frac{1}{6}C_{1111}\eta_1^3 + \frac{1}{6}(\frac{1}{2}C_{1111} + C_{1112} - \frac{1}{2}C_{2222})\eta_1^2\eta_2 + \frac{1}{2}C_{1112}\eta_1^2\eta_2 + \frac{1}{2}(\frac{1}{12}C_{1111} + \frac{1}{6}C_{1112} - \frac{1}{4}C_{1122})\eta_2\eta_6^2 \\ & - \frac{1}{2}(\frac{5}{24}C_{1111} + \frac{1}{6}C_{1112} - \frac{3}{8}C_{2222})\eta_1\eta_6^2 + \frac{1}{6}C_{1112}\eta_1^3\eta_2 + \frac{1}{24}C_{11111}\eta_1^4 + \frac{1}{24}C_{12222}\eta_2^4 + \frac{1}{4}C_{11122}\eta_1^2\eta_2^2 \\ & - \frac{1}{4}(\frac{1}{10}C_{11111} + \frac{1}{8}C_{11112} - \frac{9}{40}C_{22222})\eta_1^2\eta_6^2 + \frac{1}{24}(\frac{11}{80}C_{11111} + \frac{3}{8}C_{11112} + \frac{1}{8}C_{11122} - \frac{9}{16}C_{12222} - \frac{3}{40}C_{22222})\eta_6^4 \\ & + \frac{1}{6}(\frac{1}{2}C_{11111} + \frac{3}{2}C_{11112} + C_{11122} - \frac{3}{2}C_{12222} - \frac{1}{2}C_{22222})\eta_1\eta_2^3 + \frac{1}{4}(\frac{1}{15}C_{11111} + \frac{1}{8}C_{11112} - \frac{1}{6}C_{11122} - \frac{1}{40}C_{22222})\eta_2^2\eta_6^2 \\ & - \frac{1}{2}(\frac{13}{120}C_{11111} + \frac{1}{4}C_{11112} + \frac{1}{6}C_{11122} - \frac{3}{8}C_{12222} - \frac{3}{20}C_{22222})\eta_1\eta_2\eta_6^2, \end{aligned} \quad (6)$$

$$\begin{aligned} \Sigma_2 = & C_{12}\eta_1 + C_{11}\eta_2 + \frac{1}{2}C_{112}\eta_1^2 + \frac{1}{2}C_{222}\eta_2^2 + (C_{111} + C_{112} - C_{222})\eta_1\eta_2 - \frac{1}{2}(\frac{1}{4}C_{112} - \frac{1}{2}C_{111} + \frac{1}{4}C_{222})\eta_6^2 + \frac{1}{6}C_{1112}\eta_1^3 \\ & + \frac{1}{6}C_{2222}\eta_2^3 + \frac{1}{2}(\frac{1}{2}C_{1111} + C_{1112} - \frac{1}{2}C_{2222})\eta_1\eta_2^2 + \frac{1}{2}C_{1122}\eta_1^2\eta_2 + \frac{1}{2}(\frac{1}{12}C_{1111} + \frac{1}{6}C_{1112} - \frac{1}{4}C_{1122})\eta_1\eta_6^2 \\ & - \frac{1}{2}(\frac{1}{6}C_{1112} - \frac{7}{24}C_{1111} + \frac{1}{8}C_{2222})\eta_2\eta_6^2 - \frac{1}{4}(\frac{13}{120}C_{11111} + \frac{1}{4}C_{11112} + \frac{1}{6}C_{11122} - \frac{3}{8}C_{12222} - \frac{3}{20}C_{22222})\eta_1^2\eta_6^2 \\ & + \frac{1}{6}C_{1122}\eta_1^3\eta_2 + \frac{1}{6}C_{12222}\eta_1\eta_2^3 + \frac{1}{24}C_{11112}\eta_1^4 + \frac{1}{24}C_{22222}\eta_2^4 + \frac{1}{2}(\frac{1}{15}C_{11111} + \frac{1}{8}C_{11112} - \frac{1}{6}C_{11122} - \frac{1}{40}C_{22222})\eta_1\eta_2\eta_6^2 \\ & + \frac{1}{24}(\frac{1}{8}C_{11122} - \frac{3}{8}C_{11112} - \frac{1}{80}C_{11111} + \frac{3}{16}C_{12222} + \frac{3}{40}C_{22222})\eta_6^4 \\ & + \frac{1}{4}(\frac{1}{2}C_{11111} + \frac{3}{2}C_{11112} + C_{11122} - \frac{3}{2}C_{12222} - \frac{1}{2}C_{22222})\eta_1^2\eta_2^2 - \frac{1}{4}(\frac{1}{8}C_{12222} - \frac{9}{40}C_{11111} + \frac{1}{10}C_{22222})\eta_2^2\eta_6^2, \end{aligned} \quad (7)$$

TABLE I. Independent components of stiffness tensors.

| $C_{IJ}$                                | $C_{IJK}$  | $C_{IJKL}$   | $C_{IJKLM}$   |
|---|--|--|---|
| $C_{11}$                                | $C_{111}$  | $C_{1111}$   | $C_{11111}$   |
| $C_{12}$                                | $C_{112}$  | $C_{1112}$   | $C_{11112}$   |
| $C_{66} = \frac{1}{2}(C_{11} - C_{12})$ | $C_{222}$  | $C_{1122}$   | $C_{11122}$   |
|   | $C_{116} = 0$  | $C_{2222}$   | $C_{12222}$   |
|   | $C_{126} = 0$  | $C_{1126} = 0$   | $C_{22222}$   |
|   | $C_{166} = \frac{1}{4}(3C_{222} - 2C_{111} - C_{112})$ | $C_{1166} = \frac{1}{24}(-5C_{1111} - 4C_{1112} + 9C_{2222})$            | $C_{11116} = 0$   |
|   | $C_{266} = \frac{1}{4}(2C_{111} - C_{222} - C_{112})$  | $C_{1222} = \frac{1}{2}(C_{1111} + 2C_{1112} - C_{2222})$                | $C_{11126} = 0$   |
|   | $C_{122} = C_{111} + C_{112} - C_{222}$                | $C_{1266} = 0$   | $C_{11166} = \frac{1}{40}(-4C_{11111} - 5C_{11112} + 9C_{22222})$                             |
|   | $C_{666} = 0$  | $C_{1266} = \frac{1}{12}(C_{1111} + 2C_{1112} - 3C_{1122})$              | $C_{11222} = \frac{1}{2}(C_{11111} + 3C_{11112} + 2C_{11122} - 3C_{12222} - C_{22222})$       |
|   |  | $C_{1666} = 0$   | $C_{11226} = 0$   |
|   |  | $C_{2226} = 0$   | $C_{11266} = 0$   |
|   |  | $C_{2666} = \frac{1}{24}(7C_{1111} - 4C_{1112} - 3C_{2222})$             | $C_{11666} = 0$   |
|   |  | $C_{6666} = \frac{1}{16}(-C_{1111} - 8C_{1112} + 6C_{1122} + 3C_{2222})$ | $C_{12226} = 0$   |
|   |  |  | $C_{12666} = 0$   |
|   |  |  | $C_{16666} = \frac{1}{40}(9C_{11111} - 5C_{11222} - 4C_{22222})$                              |
|   |  |  | $C_{22226} = 0$   |
|   |  |  | $C_{22266} = \frac{1}{40}(9C_{11111} - 5C_{11222} - 4C_{22222})$                              |
|   |  |  | $C_{26666} = 0$   |
|   |  |  | $C_{66666} = \frac{1}{80}(-C_{11111} - 30C_{11112} + 10C_{11122} + 15C_{12222} + 6C_{22222})$ |

$$\begin{aligned}
\Sigma_6 = & \frac{1}{2}(C_{11} - C_{12})\eta_6 + \frac{1}{4}(2C_{111} - C_{112} - C_{222})\eta_2\eta_6 - \frac{1}{4}(2C_{111} + C_{112} - 3C_{222})\eta_1\eta_6 + \frac{1}{12}(C_{1111} + 2C_{1112} - 3C_{1122})\eta_1\eta_2\eta_6 \\
& - \frac{1}{48}(5C_{1111} + 4C_{1112} - 9C_{2222})\eta_1^2\eta_6 + \frac{1}{48}(7C_{1111} - 4C_{1112} - 3C_{2222})\eta_2^2\eta_6 - \frac{1}{96}(C_{1111} + 8C_{1112} - 6C_{1122} - 3C_{2222})\eta_6^3 \\
& - \frac{1}{240}(4C_{11111} + 5C_{11112} - 9C_{22222})\eta_1^3\eta_6 + \frac{1}{24}(9C_{11111} - 5C_{12222} - 4C_{22222})\eta_2^3\eta_6 \\
& + \frac{1}{240}(8C_{11111} + 15C_{11112} - 20C_{11122} - 3C_{22222})\eta_1\eta_2^2\eta_6 - \frac{1}{480}(C_{11111} + 30C_{11112} - 10C_{11122} - 15C_{12222} - 6C_{22222})\eta_2\eta_6^3 \\
& + \frac{1}{480}(11C_{11111} + 30C_{11112} + 10C_{11122} - 45C_{12222} - 6C_{22222})\eta_1\eta_6^3 \\
& - \frac{1}{240}(13C_{11111} + 30C_{11112} + 20C_{11122} - 45C_{12222} - 18C_{22222})\eta_1^2\eta_2\eta_6, \tag{8}
\end{aligned}$$

where  $\eta_1$ ,  $\eta_2$ , and  $\eta_6$  are the in-plane components of the Lagrangian strain tensor defined relative to the orientation of monolayer MoS<sub>2</sub> shown in Fig. 2.

We now consider several special deformation states that simplify the expressions for the general nonlinear in-plane elastic response, which we will now refer to being in uniaxial strain. The elastic response of monolayer MoS<sub>2</sub> is calculated for these special states. With reference to Fig. 2, a state of uniaxial strain in the  $x_1$ -direction is characterized by  $\eta_1 \geq 0$  and  $\eta_2 = \eta_6 = 0$ . The corresponding elastic response gives  $\Sigma_1 \geq 0$ ,  $\Sigma_2 \geq 0$ , where  $\Sigma_2$  is the lateral constraint stress for this configuration, which is the stress required to maintain zero strain in the lateral direction; symmetry dictates that  $\Sigma_6 = 0$ . Similarly, we consider a state of uniaxial strain in the  $x_2$ -direction. Finally, we consider a state of equibiaxial strain for which  $\eta_1 = \eta_2 = \eta \geq 0$  and  $\eta_6 = 0$  which results in  $\Sigma_1 = \Sigma_2 \geq 0$  and  $\Sigma_6 = 0$ . The deformation gradient tensors for the three deformation states, respectively, are

$$\mathbf{F}_1 = \begin{bmatrix} \lambda_1 & 0 \\ 0 & 1 \end{bmatrix}, \quad \mathbf{F}_2 = \begin{bmatrix} 1 & 0 \\ 0 & \lambda_2 \end{bmatrix}, \quad \mathbf{F}_{bi} = \begin{bmatrix} \lambda_{bi} & 0 \\ 0 & \lambda_{bi} \end{bmatrix}, \tag{9}$$

where the stretch ratio  $\lambda_1$  is the ratio of the deformed length of the unit cell in the  $x_1$ -direction to the reference length,  $\lambda_2$  is defined analogously for deformation in the  $x_2$  direction, and for the equibiaxial case  $\lambda_{bi} = \lambda_1 = \lambda_2$ .

For uniaxial strain in the  $x_1$ -direction, the general stress-strain response simplifies to

$$\Sigma_1 = C_{11}\eta_1 + \frac{1}{2}C_{111}\eta_1^2 + \frac{1}{6}C_{1111}\eta_1^3 + \frac{1}{24}C_{11111}\eta_1^4, \tag{10}$$

$$\Sigma_2 = C_{12}\eta_1 + \frac{1}{2}C_{112}\eta_1^2 + \frac{1}{6}C_{1112}\eta_1^3 + \frac{1}{24}C_{11112}\eta_1^4, \tag{11}$$

$$\Sigma_6 = 0. \tag{12}$$

For uniaxial strain in the  $x_2$ -direction there results

$$\begin{aligned}
\Sigma_1 = & C_{12}\eta_2 + \frac{1}{2}(C_{111} - C_{222} + C_{112})\eta_2^2 \\
& + \frac{1}{12}(C_{1111} + 2C_{1112} - C_{2222})\eta_2^3 + \frac{1}{24}C_{12222}\eta_2^4, \tag{13}
\end{aligned}$$

$$\Sigma_2 = C_{11}\eta_2 + \frac{1}{2}C_{222}\eta_2^2 + \frac{1}{6}C_{2222}\eta_2^3 + \frac{1}{24}C_{22222}\eta_2^4, \tag{14}$$

$$\Sigma_6 = 0. \tag{15}$$

For the biaxial strain state there results

$$\begin{aligned}
\Sigma_1 = \Sigma_2 = & (C_{11} + C_{12})\eta + \frac{1}{2}(2C_{111} - C_{222} + 3C_{112})\eta^2 \\
& + \frac{1}{6}\left(\frac{3}{2}C_{1111} + 4C_{1112} - \frac{1}{2}C_{2222} + 3C_{1122}\right)\eta^3 \\
& + \frac{1}{24}(3C_{11111} + 10C_{11112} - 5C_{12222} \\
& + 10C_{11122} - 2C_{22222})\eta^4, \tag{16}
\end{aligned}$$

$$\Sigma_6 = 0. \tag{17}$$

It is significant to note that all 14 elastic constants appear in the stress versus strain constitutive relationships for the three special cases collectively. Thus, the values of the elastic constants can be determined by fitting to the stress versus strain response as calculated from first-principles calculations.

In addition, we consider the elastic behavior of MoS<sub>2</sub> under conditions of uniaxial stress as a means to verify the internal consistency of the higher-order continuum theory. Uniaxial stress in the  $x_1$ -direction is characterized by  $\Sigma_1 \geq 0$ ,  $\Sigma_2 = 0$  with  $\eta_1 \geq 0$  and  $\eta_2 \leq 0$  due to Poisson contraction. Uniaxial stress in the  $x_2$ -direction is defined analogously.

### III. FIRST-PRINCIPLES CALCULATIONS OF ELASTIC RESPONSE

We use density functional theory (DFT) to calculate the elastic response for the three special deformation states. The DFT calculations are performed with the VASP software package<sup>27-31</sup> using the projector augmented wave method and both the local density approximation<sup>32</sup> (LDA) and the generalized gradient approximation<sup>31,33</sup> (GGA) at 0 K.

A unit cell of one molybdenum atom and two sulfur atoms is employed assuming a separation distance of 61.5 Å between MoS<sub>2</sub> monolayers. The  $k$ -point grid is  $13 \times 13 \times 3$  with a cutoff energy of 500 eV. The undeformed equilibrium state is determined through an energy and stress minimization as a function of the in-plane lattice vector and out-of-plane sulfur atom heights. The equilibrium configuration is determined to be a spacing of 3.122 Å between molybdenum atoms and an out-of-plane distance of 1.557 Å between a plane of sulfur atoms and the intermediate plane of molybdenum atoms. These results are consistent with experimentally determined lattice spacing of 3.16 Å between Mo atoms and 1.59 Å out-of-plane height for S atoms in a bulk MoS<sub>2</sub> crystal.<sup>34</sup> The stress components computed in VASP are in terms of true stress, or

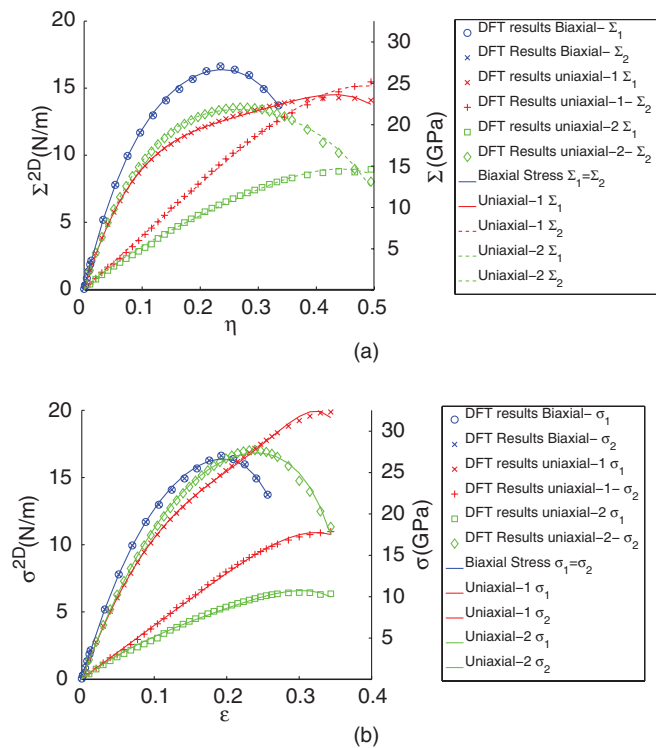


FIG. 3. (Color online) (a) The least-squares curve fit to DFT data using the LDA functional of three prescribed deformation states. Quantities are plotted in second Piola-Kirchhoff stress and Lagrangian strain. Symbols depict calculated data and lines indicate least-squares fits. (b) The same data converted to true stress and true strain.

Cauchy stress  $\sigma$ , in units of force per area on the cross-sectional edges of the unit cell. For a 2D material, it is appropriate to express the stress in terms of force per length of the edge; this is obtained from the product of the the stress components calculated from VASP and the interlayer spacing of 61.5 Å.

The relation between the true stress and second Piola-Kirchhoff (P-K) stress  $\Sigma$  is given as

$$\Sigma = J \mathbf{F}^{-1} \sigma (\mathbf{F}^{-1})^T, \quad (18)$$

where  $J$  is the determinant of the deformation gradient tensor  $\mathbf{F}$ .<sup>35</sup> In this work, we did not explore the possibility of finite wave-vector instabilities which might be relevant at large strains. For example, in graphene a phonon instability of the  $K$  mode occurs for sufficiently large equibiaxial strain.<sup>36</sup>

To calculate the elastic response of a given deformation state, the unit cell is determined according to the deformed lattice vectors  $\mathbf{a}'_i$  which are functions of the applied  $\mathbf{F}$ . The molybdenum and sulfur atoms are relaxed in the strained unit cell into the minimum potential energy configuration both in and out of the plane. A series of simulations is performed for both uniaxial strain cases as well as the equibiaxial strain case, beginning with strains within the linear-elastic regime and finishing with strains beyond that corresponding to the intrinsic (i.e., maximum) stress.

The results of the VASP simulations are shown in Fig. 3(a) where the second Piola-Kirchhoff stress is plotted as a function of the Lagrangian strain and in Fig. 3(b) the true stress is plotted as a function of the true strain. True (i.e., Cauchy) stress

TABLE II. Nonzero independent elastic constant fit to the LDA functional DFT data of monolayer MoS<sub>2</sub> relating the second Piola-Kirchhoff stress tensor to the Lagrangian strain deformation state. The SOEC, TOEC, FOEC, and FFOEC (second-, third-, fourth-, and fifth-order elastic constants, respectively) are tabulated.

| SOEC (N/m)     | TOEC (N/m)        | FOEC (N/m)        | FFOEC (N/m)            |
|----------------|-------------------|-------------------|------------------------|
| $C_{11} = 140$ | $C_{111} = -1300$ | $C_{1111} = 8770$ | $C_{11111} = -29\,830$ |
| $C_{12} = 40$  | $C_{112} = -1090$ | $C_{1112} = 440$  | $C_{11112} = -4340$    |
|                | $C_{222} = -30$   | $C_{1122} = -230$ | $C_{11122} = -230$     |
|                |                   | $C_{2222} = 5870$ | $C_{12222} = -8450$    |
|                |                   |                   | $C_{22222} = -18\,930$ |

is calculated based on Eq. (18) and the true strain is given as  $\varepsilon = \ln(\lambda)$ . The calculated DFT results are highlighted as symbols. The red symbols represent calculations for uniaxial strain in the  $x_1$ -direction, with the  $+$  and  $\times$  symbols indicating the lateral constraint and normal stresses as a function of prescribed strain  $\eta$ , respectively. The green symbols represent calculations for uniaxial strain in the  $x_2$ -direction, with the  $\square$  and  $\diamond$  symbols indicating the lateral constraint and normal stresses, respectively. The blue  $\otimes$  symbols represent the equibiaxial stress ( $\Sigma_1 = \Sigma_2$ ) in the  $x_1$ - and  $x_2$ -directions.

The values of the 14 independent components of the stiffness tensors are determined by least-squares curve fitting of Eqs. (10)–(17) to the corresponding DFT calculations. The results, shown as solid colored lines in Fig. 3, demonstrate that the higher-order continuum formulation accurately describes the calculated stress-strain response up to approximately 0.30 Lagrangian strain or 0.25 true strain. The resulting 14 independent elastic constants for monolayer MoS<sub>2</sub> are tabulated in Table II. For the linear-elastic regime at small strains, the Young's modulus is  $E^{2D} = 129$  N/m and the in-plane Poisson's ratio is  $\nu = 0.29$ .

A fifth-order expansion of the strain energy density function captures the anisotropy of 2D MoS<sub>2</sub> and the elastic instability used to predict failure of the material. The appropriateness of the fifth-order fit is verified by comparing the root-mean-square (rms) deviation defined as  $\sqrt{SSE/n}$ , where  $SSE$  is the sum of squares error and  $n$  is the number of data points used in the fit. Comparing the rms deviation for the 234 data points of stress and strain, a third-order elastic constant expansion results in a rms deviation of 1.404 N/m, a fourth-order approximation results in 0.462 N/m, and the fifth-order approximation results in a 0.145 N/m rms deviation. The third- and fourth-order approximations can not capture both the linear response and the peak stress at finite strains in the same fit. The third- and fourth-order fits underpredict the Young's modulus as 65 and 104 N/m, respectively. The fifth-order approximation captures the relevant behavior of 2D MoS<sub>2</sub> under tension including the linear-elastic response and the elastic instability used to predict fracture.

It is interesting to note that the anisotropy of MoS<sub>2</sub> is very prominent in Fig. 3(a) comparing the resulting second Piola-Kirchhoff stresses as a result of uniaxial strains in the  $x_1$ - and  $x_2$ -directions. Along the  $x_1$ -direction, as defined in Fig. 1, the second Piola-Kirchhoff lateral constraint stress becomes higher than the normal stress. The true stress measure, in Fig. 3(b), reveals that this phenomenon is a result of the

TABLE III. Nonzero independent elastic constant fits to the PBE functional DFT data of monolayer MoS<sub>2</sub> relating the second Piola-Kirchhoff stress tensor to the Lagrangian strain deformation state. The SOEC, TOEC, FOEC and FFOEC (second-, third-, fourth- and fifth-order elastic constants, respectively) are tabulated.

| SOEC (N/m)     | TOEC (N/m)        | FOEC (N/m)        | FFOEC (N/m)          |
|----------------|-------------------|-------------------|----------------------|
| $C_{11} = 130$ | $C_{111} = -1200$ | $C_{1111} = 7800$ | $C_{11111} = -26460$ |
| $C_{12} = 40$  | $C_{112} = -1010$ | $C_{1112} = 580$  | $C_{11112} = -4200$  |
|                | $C_{222} = -60$   | $C_{1122} = -50$  | $C_{11122} = -800$   |
|                |                   | $C_{2222} = 5760$ | $C_{12222} = -6880$  |
|                |                   |                   | $C_{22222} = -21300$ |

reference area choice. In a system composed of one type of atom, such as graphene, this behavior has not been observed.<sup>9</sup>

The calculations are repeated using a projector augmented wave with a generalized gradient approximation (GGA), the Perdew-Burke-Ernzerhof (PBE), functional in VASP. The unit cell remains one molybdenum atom and two sulfur atoms and a separation distance of 61.5 Å between MoS<sub>2</sub> monolayers. The  $k$ -point grid remains  $13 \times 13 \times 3$  with a cutoff energy of 500 eV. The undeformed equilibrium state is determined through an energy and stress minimization as a function of the molybdenum atom spacing and out-of-plane sulfur atom heights. The equilibrium configuration is determined to be a spacing of 3.182 Å between molybdenum atoms and an out-of-plane distance of 1.563 Å between a plane of sulfur atoms and the intermediate plane of molybdenum atoms for the PBE functional. The resulting higher-order elastic constants are shown in Table III and the graphs are shown in Figure 4.

The PBE functional results fit to the higher-order nonlinear elastic constants predict a Young's modulus of  $E = 118$  N/m and a Poisson's ratio of  $\nu = 0.31$ . At strains above 20%, the difference in stress measures for LDA and PBE is approximately 15%. The calculations with LDA predict an elastic instability at  $\eta = 23.4\%$  and  $\Sigma = 27$  N/m, while the PBE calculations predict an elastic instability as  $\eta = 23.2\%$  and  $\Sigma = 24$  N/m.

We verify in two ways that our calculations and constitutive model are correct and internally self-consistent. First, we reproduce our VASP calculations of the elastic response under all five deformation states considered herein with both the ABINIT and QUANTUM ESPRESSO DFT software packages. The results from all three software packages are quantitatively consistent with each other for the PBE approximation, thus verifying the DFT calculations. Second, we demonstrate that the DFT calculations and the continuum constitutive model are internally self consistent, individually for the LDA and PBE approximations. To do so, we first calculated the elastic response for the equibiaxial and the two uniaxial strain deformation states using DFT. Then, we determined the 14 independent elastic constants of the continuum fifth-order elastic constitutive description by fitting to the DFT results of the equibiaxial and the two uniaxial strain deformation states. We then predicted the elastic response under the two states of uniaxial stress using the continuum model. We then calculated the elastic response for the two states of uniaxial stress via DFT. The continuum predictions are compared to the DFT calculations in Fig. 5(a) for the LDA approximation

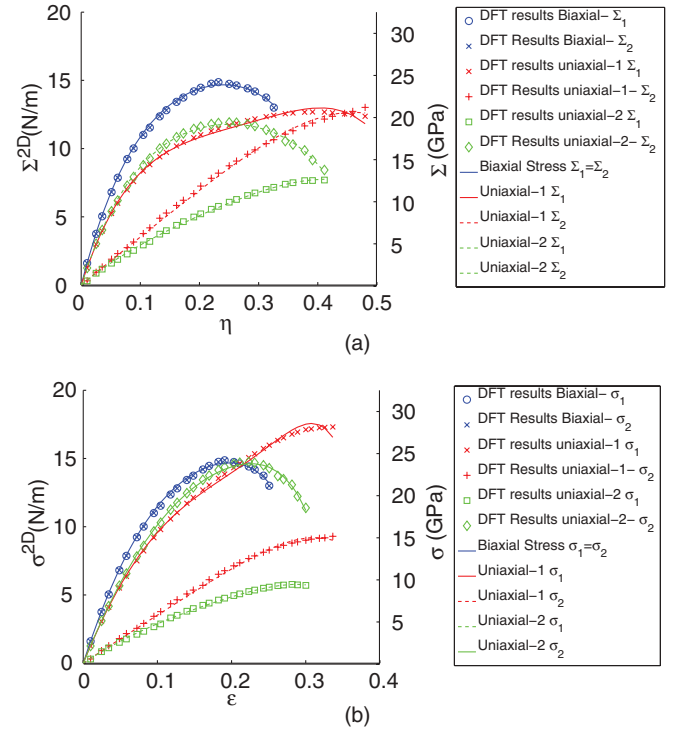


FIG. 4. (Color online) (a) The least-squares curve fit to DFT data using the PBE functional of three prescribed deformation states. Quantities are plotted in second Piola-Kirchhoff stress and Lagrangian strain. Symbols depict calculated data and lines indicate least-squares fits. (b) The same data converted to true stress and true strain.

and Fig. 5(b) for the PBE approximation. There is a very good agreement between the predictions and the calculations, thus verifying the internal consistency of the multiscale atomistic (DFT) and continuum constitutive model. It bears emphasis that the 14 elastic constants are determined by fitting to DFT results from only the equibiaxial and uniaxial strain states for each approximation; the DFT results for the two uniaxial stress deformation states were not used in the curve-fitting process.

For completeness, we now discuss the details of the DFT calculation under uniaxial stress conditions. The uniaxial stress DFT calculations are achieved by relaxing the  $\hat{e}_2$ -components of the  $\mathbf{a}_1$ - and  $\mathbf{a}_2$ -lattice vectors for uniaxial stress in the  $x_1$ -direction. The uniaxial stress state in the  $x_2$  direction is achieved analogously by relaxation of the  $\hat{e}_1$ -components. Li<sup>37</sup> performs uniaxial stress calculations that are not consistent with our results. However, our results have been verified using three *ab initio* codes (i.e., VASP, ABINIT, and QUANTUM ESPRESSO), and a direct comparison to Li's results will be made in a forthcoming publication.<sup>38</sup>

#### IV. EXPERIMENTAL METHODS

Following the approach and procedures of Lee *et al.*<sup>4</sup> the specimens are fabricated on a silicon substrate with a 300-nm epilayer of SiO<sub>2</sub>. We introduce an array of circular wells with 500-nm diameter and 500-nm depth, via reactive ion etching, into the substrate following patterning via electron beam lithography. Then, MoS<sub>2</sub> is mechanically exfoliated onto

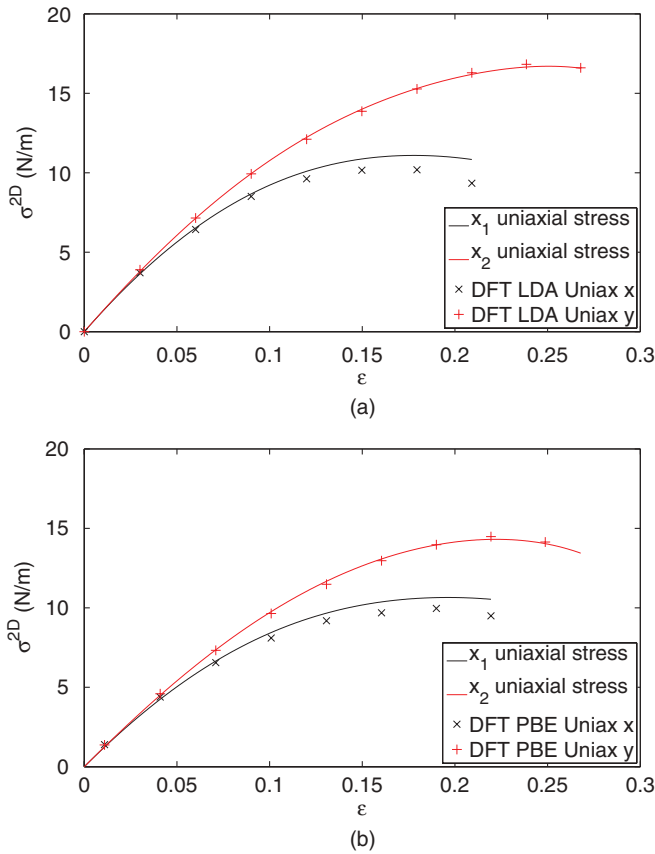


FIG. 5. (Color online) Plotted above are the uniaxial stress calculations based upon DFT with a LDA functional (a) and a PBE functional (b). The + and × data points represent the data calculated for a uniaxial stress state in the  $x_1$  and  $x_2$  directions, respectively. The red and black lines represent the least-squares curve fit prediction of the stress-strain curve for uniaxial stress in the  $x_1$  and  $x_2$  directions, respectively. The data are plotted in true stress and true strain.

the substrate. The individual flakes of MoS<sub>2</sub>, with sizes up to 4 μm by 8 μm, are randomly distributed atop the substrate and are large enough to cover several adjacent wells.

The nanoindentation experiments performed in this study offer several advantages over mechanical tests performed on nanotube structures. First, the sample geometry is precisely defined and the 2D structure is less sensitive to material or substrate defects. The circular freestanding monolayers of MoS<sub>2</sub> are effectively clamped around the periphery via van der Waals interactions with the substrate, which serves to constrain both radial and out-of-plane displacements. Thus, the boundary conditions are well defined and repeatable, whereas it is much more difficult to obtain such boundary conditions when loading nanotube configurations.

We use optical microscopy to identify candidate monolayer MoS<sub>2</sub> sheets suspended above wells, as seen in Fig. 6(a). Then, an AFM (XE-100, Park Systems) in noncontact mode confirms the monolayer thickness to be 0.615 nm.<sup>39</sup> Suspended monolayers are imaged in noncontact mode to determine the center of the membrane. The monolayer films are then indented at their centers with the AFM to determine the force-displacement response as well as the breaking force.

The AFM tip is a diamond cube corner on a silicon cantilever fabricated by MicroStar Technologies; standard silicon AFM tips are not used because the load levels can cause fracture of the tip prior to rupture of the monolayer MoS<sub>2</sub>. The tip radius, measured before and after indentation using a transmission electron microscope (TEM), is 26 nm. The AFM cantilever is calibrated against a reference cantilever for accurate determination of its stiffness.<sup>40</sup> Indentations are performed on 12 suspended membranes from one flake of MoS<sub>2</sub> that can be seen in Fig. 6. Each monolayer MoS<sub>2</sub> membrane is loaded and unloaded several times at a prescribed AFM tip displacement rate of 1.25 μm/s. Eight of the membranes exhibit significant hysteresis of the force-displacement response, indicating that the van der Waals interactions are not sufficient to preclude slipping at the periphery of the suspended membranes; data from these membranes are not included in subsequent analysis. Four of the membranes exhibit negligible hysteresis. The depth of the indent load-unload cycles is increased in 30–50 nm increments until rupture of the membrane is recorded, characterized by the tip plunging through the membrane and a sudden diminution of the force. A typical set of data in Fig. 7 shows two loading-unloading curves in blue and green, demonstrating the negligible hysteresis. Subsequently, in the red curve, the membrane is loaded to rupture shown by the × symbol. The average breaking force of the four membranes is 1500 nN with a standard deviation of 300 nN.

The force-displacement data are analyzed to characterize the elastic response of monolayer MoS<sub>2</sub>. A semiempirical formula approximates the relationship between force and displacement for an axisymmetric membrane under a central point load as<sup>4</sup>

$$F = \sigma_0(\pi a) \left( \frac{\delta}{a} \right) + E(q^3 a) \left( \frac{\delta}{a} \right)^3, \quad (19)$$

where  $F$  is the applied force on the AFM tip,  $\delta$  is the load point deflection,  $a$  is the membrane radius,  $E$  and  $\sigma_0$  are the 2D Young's modulus and prestress in the film, respectively, and  $q = (1.05 - 0.15\nu - 0.16\nu^2)$ , and  $\nu = 0.29$  the Poisson's ratio. The prestress and Young's modulus are determined by fitting Eq. (19) to the experimental force-displacement data. The resulting measure of stiffness is valid only as an estimate of the in-plane Young's modulus; it does not offer any insight into 3D mechanical behaviors such as bending stiffness. In this study, 26 loading curves yield an average value of  $\bar{E} = 120$  N/m with a standard deviation of 30 N/m and an average prestress of  $\bar{\sigma}_0 = 0.4$  N/m with a standard deviation of 0.2 N/m.

## V. EXPERIMENTAL VALIDATION

We now discuss results of a detailed finite element analysis (FEA) of the indentation of the circular monolayer MoS<sub>2</sub> membrane and compare the results to the experimental data. The FEA simulation employs the higher-order nonlinear elastic constitutive behavior of Eqs. (6)–(8) as well as the elastic constants in Table II that have been implemented into a user material (UMAT) subroutine<sup>10</sup> for use with the commercially available finite element program ABAQUS.<sup>41</sup> This implementation is valid for use in membrane elements, which

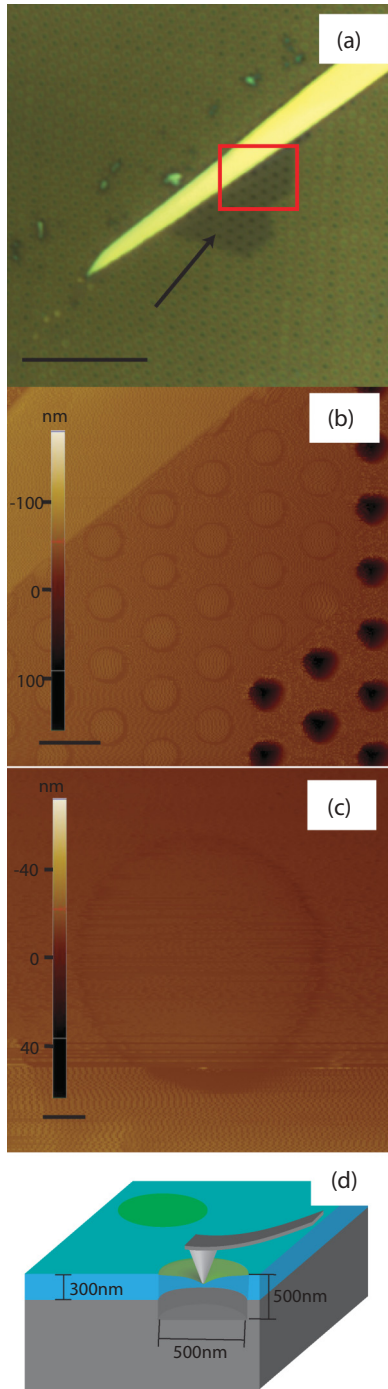


FIG. 6. (Color online) Suspended MoS<sub>2</sub> on SiO<sub>2</sub> substrate imaged via optical microscopy (a) and AFM (b) and (c). The arrow in image (a) points to a flake of monolayer MoS<sub>2</sub>; (b) shows the AFM image of the area highlighted in red in (a); the scale bars in (a), (b), and (c) are 10 μm, 5 μm, and 100 nm, respectively; and (d) shows the experimental setup graphically.

implies that the bending stiffness of the MoS<sub>2</sub> is vanishingly small compared to the in-plane stiffness. This assumption is valid when the radius of curvature of the deformed MoS<sub>2</sub> monolayer is much greater than the distance between nearest atomic neighbors. Specifically for these simulations, the smallest radius of curvature in the MoS<sub>2</sub> is the 26 nm of the indenter tip and the interatomic distance is 3.16 Å.

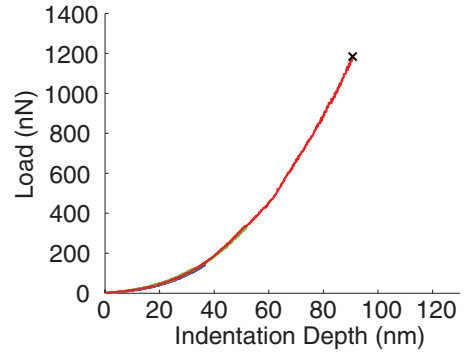


FIG. 7. (Color online) Typical loading-unloading curve for a monolayer MoS<sub>2</sub> membrane. The blue and green curves include both the loading and unloading data points. There is no evidence of hysteresis. The red curve ends in abrupt fracture of the membrane, marked by the × symbol.

The circular membrane of diameter 500 nm is modeled with 9575 four-node membrane elements and is clamped to inhibit displacements at its periphery and loaded at its center with a frictionless rigid sphere of radius 26 nm. An equibiaxial prestress is set to 0.42 N/m, the average measure of prestress from AFM nanoindentations. The simulation is performed in approximately 900 time increments equating to an average of 1.2 nm of indenter displacement per increment. The FEA formulation requires 3D stress and modulus measures as well as a well-defined membrane thickness, so we perform the computations using the derived 3D quantities. However, we report the results in terms of the intrinsic 2D quantities.

Figure 8 shows the simulated force-displacement curve at the center of the membrane for both the LDA and PBE approximations, which are in good agreement with experimental results from AFM nanoindentations. The close agreement between the results from the finite element model based on first-principles data and the nanoindentation curve is a testament to the validity of the experimental and theoretical framework that comprise this study.

Figure 9 shows the details of the stress concentration in the MoS<sub>2</sub> monolayer under the indenter tip. At very

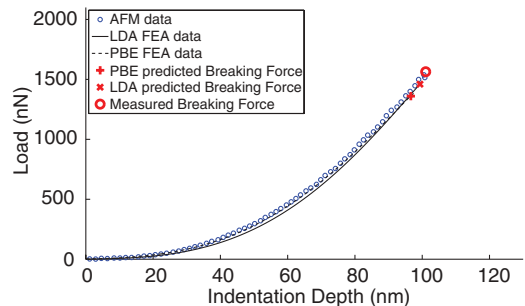


FIG. 8. (Color online) Comparison of the multiscale finite element models based on first-principles data represented by the solid and dashed lines for LDA and PBE fits, respectively. The AFM data are represented by small open circle symbols. The point at which fracture occurs in the model is represented with a + symbol for the LDA fit and a × symbol for the PBE fit. The measured breaking force from AFM nanoindentation is represented by the red large open circle symbol.

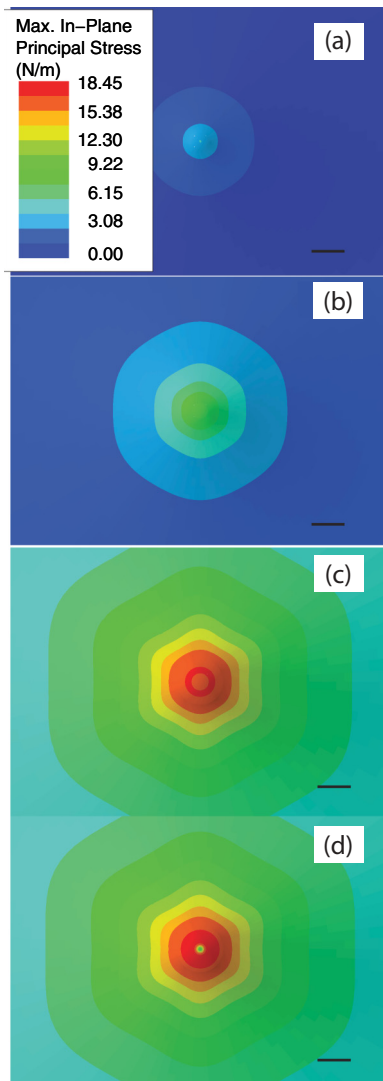


FIG. 9. (Color online) ABAQUS FEA contours showing maximum principal stress at each integration point under the spherical rigid indenter at indentation depths of (a) 6, (b) 63, (c) 98, and (d) 101 nm. The scale bars in (a)–(d) are 30 nm.

shallow indentation depths, the stress state is axisymmetric [cf. Fig. 9(a)], consistent with elastic isotropy at small strains. At an intermediate indentation depth in Fig. 9(b), the stress state begins to develop a sixfold rotation symmetry, which becomes fully developed at large indentation depths of Fig. 9(c). Thus, monolayer MoS<sub>2</sub> develops an elastic anisotropy with a sixfold rotation symmetry at finite strains of an approximate equibiaxial nature, consistent with the  $D_{3h}$  point group of the hexagonal lattice. The deformation state in the very center of the indented region experiences equibiaxial deformation, so that according to Fig. 3(a) the LDA data, the peak stress the MoS<sub>2</sub> can withstand is 16.5 N/m, a Lagrangian strain of about 0.23. At larger equibiaxial strains, the stress will decrease and the deformation state will be unstable because of the negative local tangent modulus leading to strain softening. Figure 9(d) shows the monolayer MoS<sub>2</sub> at the state when the stress in the very center has begun to decrease. The FEA simulation

becomes unable to converge to equilibrium solutions at an indentation depth past 102 nm, where force on the indenter tip in the first-principles FEA model is 1490 nN for the LDA least-squares fit and 1360 nN for the PBE least-squares fit, well within the experimental uncertainty of the measurements. The 95% confidence interval for the experimental breaking force is 1350–1650 nN. A smaller degree of uncertainty in experimental measurements would lend insight into which approximation closer represents the mechanical properties of MoS<sub>2</sub>.

## VI. CONCLUSIONS

We have calculated using DFT the elastic response of monolayer MoS<sub>2</sub> for in-plane conditions of uniaxial strain and equibiaxial strain. The strains range from infinitesimal values to finite values beyond that corresponding to the intrinsic (i.e., maximum) stress. In addition, we derived the framework for a thermodynamically rigorous nonlinear elastic constitutive relationship for arbitrary in-plane deformation by expanding the strain energy density in a Taylor series in powers of Lagrangian strain truncated after the fifth power. There are 14 independent components of the resulting stiffness tensors. The values of these components are determined by fitting to the DFT results. The resulting multiscale continuum constitutive relationship is nonlinear and anisotropic, although the nonlinearity does not manifest itself until a strain beyond about 0.05 and the anisotropy becomes significant only after a strain of about 0.1. AFM nanoindentation experiments performed on circular suspended monolayers of MoS<sub>2</sub> provide experimental evidence of intrinsic strength and in-plane Young's modulus. A detailed finite element model (FEM) of the experimental configuration was performed with ABAQUS along with a user material (UMAT) which incorporated the continuum constitutive model for use in membrane elements. The predicted force versus displacement response as well as the force at rupture of the MoS<sub>2</sub> film correspond closely to the experimental values. This study bridges three main gaps that hinder understanding of material properties: DFT to FEM, experimental results to DFT, and the nanoscale to the microscale. In bridging these three gaps, the experimental results validate the DFT calculations and the multiscale constitutive model.

Our results show that MoS<sub>2</sub> is a strong and flexible crystal. The maximum stress at the point of fracture is the intrinsic strength of the MoS<sub>2</sub>,  $\sigma_{\text{int}} = 16.5$  N/m, as confirmed with finite element analysis implementation of the nonlinear elastic constants. When assuming a monolayer thickness of  $t = 0.615$  nm, the 3D intrinsic strength of MoS<sub>2</sub> is  $\sigma_{\text{int}}^{3D} = 26.8$  GPa. The in-plane Young's modulus suitable for conditions of infinitesimal strains is  $E = 16.5$  N/m, or  $E^{3D} = 210$  GPa, which is consistent with the experimental results of Bertolazzi.<sup>11</sup> The in-plane Poisson's ratio suitable for conditions of infinitesimal strains as calculated using DFT is  $\nu = 0.29$ . It is interesting to note that Griffith<sup>42</sup> predicts the intrinsic strength of a material to be  $\sigma_{\text{int}} \approx E/9$ , whereas experimental and DFT results suggest  $\sigma_{\text{int}} \approx E/8$  in accordance with studies measuring the intrinsic strength of graphene.<sup>4</sup>

## ACKNOWLEDGMENT

The authors would like to acknowledge support from the National Science Foundation Grants No. CMMI-0927891 and No. CMMI-1150795, the National Research Foundation of

Korea (Basic Science Research program Grant No. KRF-2011-0014209), and the Center for Advanced Soft Electronics under the Global Frontier Research Program (Grant No. 2011-0031629) of the Ministry of Education, Science and Technology, Korea.

- 
- <sup>1</sup>R. Peierls, *Ann. Inst. Henri Poincaré* **5**, 177 (1935).  
<sup>2</sup>K. S. Novoselov, A. K. Geim, S. V. Morozov, D. Jiang, Y. Zhang, S. V. Dubonos, I. V. Grigorieva, and A. A. Firsov, *Science* **306**, 666 (2004).  
<sup>3</sup>A. Geim and K. Novoselov, *Nat. Mater.* **6**, 183 (2007).  
<sup>4</sup>C. Lee, X. Wei, J. W. Kysar, and J. Hone, *Science* **321**, 385 (2008).  
<sup>5</sup>K. F. Mak, C. Lee, J. Hone, J. Shan, and T. F. Heinz, *Phys. Rev. Lett.* **105**, 136805 (2010).  
<sup>6</sup>C. Neto and K. Novoselov, *Mater. Express*, **1**, 10 (2011).  
<sup>7</sup>K. S. Novoselov, D. Jiang, F. Schedin, T. Booth, V. Khotkevich, S. Morozov, and A. Geim, *Proc. Natl. Acad. Sci. USA* **102**, 10451 (2005).  
<sup>8</sup>S. Jiménez Sandoval, D. Yang, R. F. Frindt, and J. C. Irwin, *Phys. Rev. B* **44**, 3955 (1991).  
<sup>9</sup>X. Wei, B. Fragneaud, C. A. Marianetti, and J. W. Kysar, *Phys. Rev. B* **80**, 205407 (2009).  
<sup>10</sup>X. Wei and J. W. Kysar, *Int. J. Solids Struct.* **49**, 3201 (2012).  
<sup>11</sup>S. Bertolazzi, J. Brivio, and A. Kis, *ACS Nano* **5**, 9703 (2011).  
<sup>12</sup>B. Radisavljevic, A. Radenovic, J. Brivio, V. Giacometti, and A. Kis, *Nat. Nanotechnol.* **6**, 147 (2011).  
<sup>13</sup>A. Molina-Sánchez and L. Wirtz, *Phys. Rev. B* **84**, 155413 (2011).  
<sup>14</sup>L. Scandella, A. Schumacher, N. Kruse, R. Prins, E. Meyer, R. Lüthi, L. Howald, and H.-J. Güntherodt, *Thin Solid Films* **240**, 101 (1994).  
<sup>15</sup>A. Schumacher, L. Scandella, N. Kruse, and R. Prins, *Surf. Sci. Lett.* **289**, L595 (1993).  
<sup>16</sup>D. Killeffer, *Molybdenum Compounds, Their Chemistry and Technology* (Interscience, New York, 1952).  
<sup>17</sup>A. Kis, D. Mihailovic, M. Remskar, A. Mrzel, A. Jesih, I. Piwonski, A. Kulik, W. Benoît, and L. Forró, *Adv. Mater.* **15**, 733 (2003).  
<sup>18</sup>A. Splendiani, L. Sun, Y. Zhang, T. Li, J. Kim, C. Chim, G. Galli, and F. Wang, *Nano Lett.* **10**, 1271 (2010).  
<sup>19</sup>A. Kuc, N. Zibouche, and T. Heine, *Phys. Rev. B* **83**, 245213 (2011).  
<sup>20</sup>S. Lebègue and O. Eriksson, *Phys. Rev. B* **79**, 115409 (2009).  
<sup>21</sup>K. K. Kam and B. A. Parkinson, *J. Phys. Chem.* **86**, 463 (1982).  
<sup>22</sup>Y. Kadowaki, K. Aika, H. Kondoh, and H. Nozoye, *Surf. Sci.* **287-288**, 396 (1993).  
<sup>23</sup>J. F. Nye, *Physical Properties of Crystals: Their Representation by Tensors and Matrices*, Oxford Science Publications (Clarendon, Oxford, 1985).  
<sup>24</sup>D. Xiao, G. B. Liu, W. Feng, X. Xu, and W. Yao, *Phys. Rev. Lett.* **108**, 196802 (2012).  
<sup>25</sup>F. G. Fumi, *Phys. Rev.* **86**, 561 (1952).  
<sup>26</sup>T. S. G. Krishnamurty, *Acta Crystallogr.* **16**, 839 (1963).  
<sup>27</sup>G. Kresse and J. Hafner, *Phys. Rev. B* **47**, 558 (1993).  
<sup>28</sup>G. Kresse and J. Hafner, *Phys. Rev. B* **49**, 14251 (1994).  
<sup>29</sup>G. Kresse and J. Furthmüller, *Comput. Mater. Sci.* **6**, 15 (1996).  
<sup>30</sup>G. Kresse and J. Furthmüller, *Phys. Rev. B* **54**, 11169 (1996).  
<sup>31</sup>J. P. Perdew, K. Burke, and M. Ernzerhof, *Phys. Rev. Lett.* **77**, 3865 (1996).  
<sup>32</sup>J. P. Perdew and A. Zunger, *Phys. Rev. B* **23**, 5048 (1981).  
<sup>33</sup>J. P. Perdew, K. Burke, and M. Ernzerhof, *Phys. Rev. Lett.* **78**, 1396 (1997).  
<sup>34</sup>T. Böker, R. Severin, A. Müller, C. Janowitz, R. Manzke, D. Voß, P. Krüger, A. Mazur, and J. Pollmann, *Phys. Rev. B* **64**, 235305 (2001).  
<sup>35</sup>M. Crisfield, *Non-linear Finite Element Analysis of Solids and Structures*, Vol. 2 (Wiley, New York, 1997).  
<sup>36</sup>C. A. Marianetti and H. G. Yevick, *Phys. Rev. Lett.* **105**, 245502 (2010).  
<sup>37</sup>T. Li, *Phys. Rev. B* **85**, 235407 (2012).  
<sup>38</sup>R. C. Cooper, C. A. Marianetti, and J. W. Kysar (unpublished).  
<sup>39</sup>A. Ayari, E. Cobas, O. Ogundadegbe, and M. Fuhrer, *J. Appl. Phys.* **101**, 014507 (2007).  
<sup>40</sup>M. Tortonese and M. Kirk, in *Society of Photo-Optical Instrumentation Engineers (SPIE) Conference Series*, edited by T. A. Michalske and M. Wendman (SPIE, Bellingham, WA, 1997).  
<sup>41</sup>SIMULIA, ABAQUS 6.11 user's manual, 2011.  
<sup>42</sup>A. A. Griffith, *R. Soc. London Philos. Trans., Ser. A* **221**, 163 (1921).